



www.sciencemag.org/cgi/content/full/science.1210268/DC1

Supporting Online Material for

Synthesized Light Transients

A. Wirth, M. Th. Hassan, I. Grguraš, J. Gagnon, A. Moulet, T.T. Luu, S. Pabst, R. Santra,
Z. A. Alahmed, A. M. Azzeer, V. S. Yakovlev, V. Pervak, F. Krausz, E. Goulielmakis*

*To whom correspondence should be addressed. E-mail: elgo@mpq.mpg.de

Published 8 September 2011 on *Science Express*
DOI: 10.1126/science.1210268

This PDF file includes:

SOM Text

Figs. S1 to S10

References (50–59)

1. Optical properties of the light field synthesizer

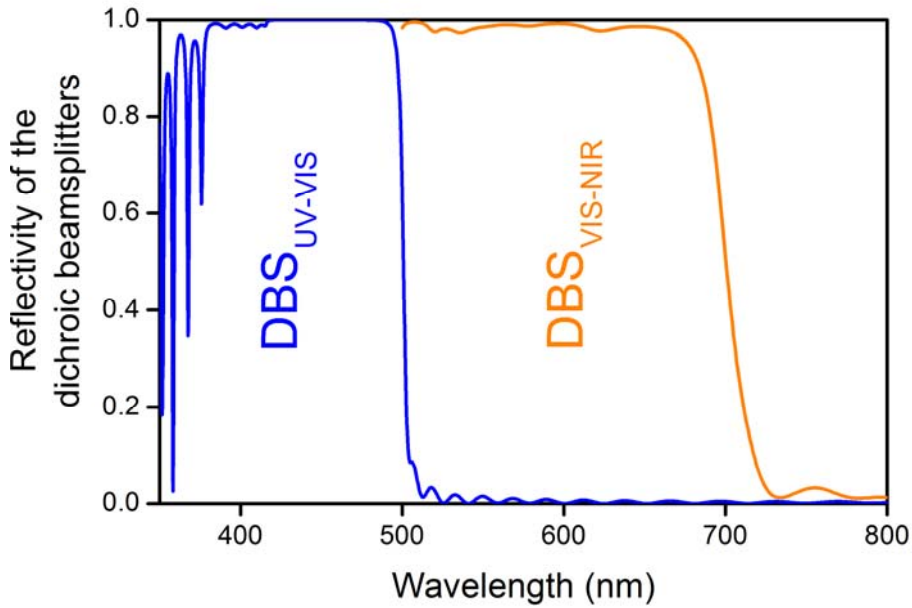


Fig. S1

Simulated reflectivity of the dichroic beamsplitters (DBS).

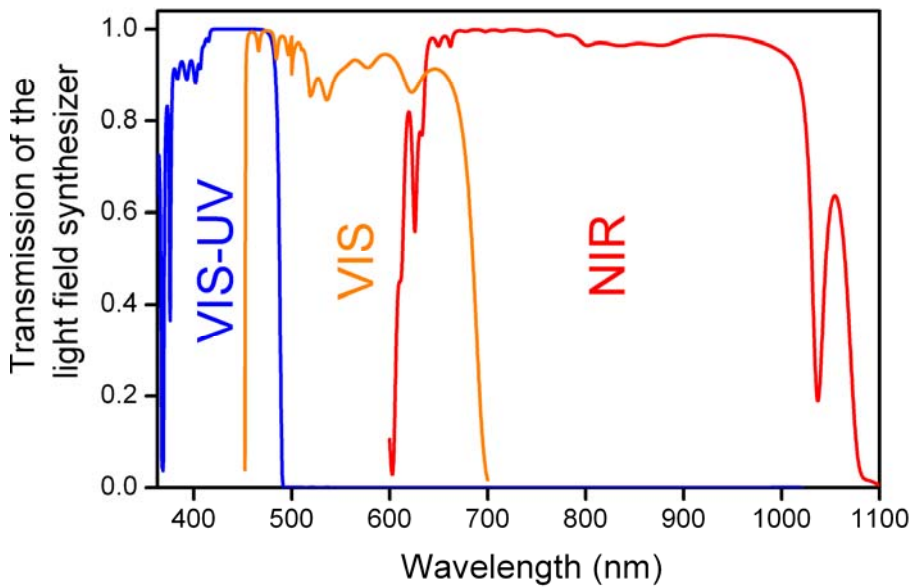


Fig. S2

Simulated total transmission of the individual channels of the optical field synthesizer. Blue (orange) line includes the reflectivity of two DBS_{UV-VIS} ($DBS_{VIS-NIR}$) and six chirped mirrors (50) $CM_{VIS/UV}$ (CM_{VIS}), whereas the red curve shows the calculated transmission based on six CM_{NIR} .



Fig. S3

Photograph of the field synthesizer in operation. Beams have been visualized by nitrogen vapor.

Intensity control with adjustable apertures

To control the relative intensities between pulses in different channels of the light field synthesizer, apertures with controllable diameters were installed into the beam path of each channel.

Despite the fact that for the experiments presented in the main text this kind of control has not been utilized, we can conveniently tune the intensity in the focus of each channel by a factor of ~ 10 . Due to this type of intensity control, spatial chirps may set in when pulses of various channels have slightly different beam diameter. However, these effects are not very critical for our experiments thanks to the extreme nonlinearity of the processes involved or studied.

For example, XUV pulse generation (or high harmonic generation in general) is confined to within a tiny fraction of the focused synthesized transient where the intensity is the highest and where all fields of the channels necessarily overlap. Moreover, at the probing stage of the light field or in a strong field experiment as reported here, the XUV attosecond pulse is focused onto a spot size that is more than 3 times smaller than that of the synthesized field, guaranteeing that the probed system is exposed to a spatially uniform field formed along the propagation axis, thereby rendering the measurement insensitive to a spatial chirp introduced by the variable apertures.

2. Attosecond Streaking and Transient Absorption experimental setup

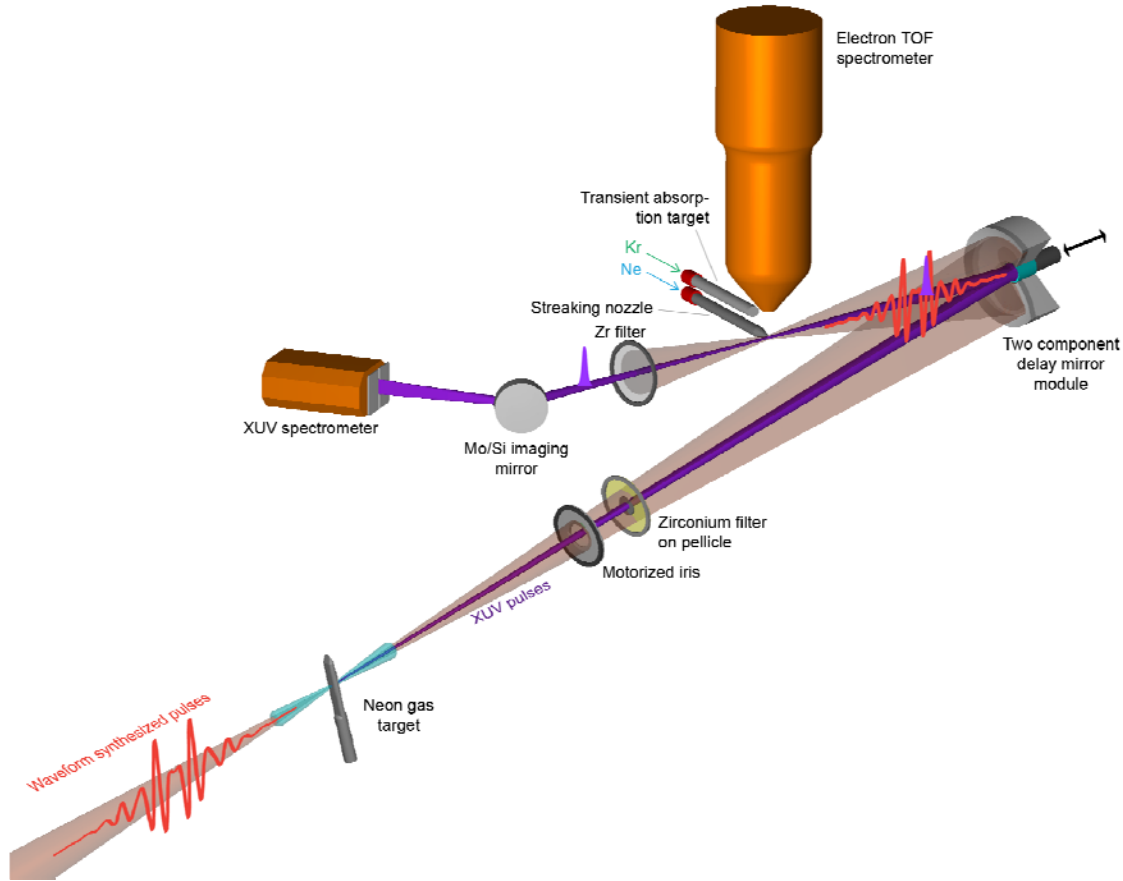


Fig. S4

Schematic diagram of the experimental setup for the characterization and application of synthesized light transients.

Light transients, synthesized by the apparatus shown in Fig. S3, are focused into a quasistatic gas cell filled with Ne (target), to generate XUV radiation by means of high order harmonic generation. The emerging, highly collimated XUV pulses are transmitted through a disk-like Zirconium (Zr) foil (150 nm) which is mounted on a thin pellicle (15 μm), while the residual visible pulses, which are also making their way through the Ne cell, are transmitted around the margins of the Zr disk to create an annular beam (see Fig. S4). A module comprised of a concave, multilayer coated inner mirror and an aluminum-coated concave annular sector (outer mirror) (34), is used to focus XUV and light transients respectively into a second gas jet or quasi static cell for either streaking or transient absorption experiments.

The inner mirror is mounted on a piezoelectric stage that allows the introduction of a delay between the light field transient and the XUV attosecond pulse along the propagation axis with nanometric precision.

A controllable iris is used to adjust the energy transported by the beam of the light transients from few microjoules (streaking) to several tens of microjoules (Transient absorption).

For streaking measurements a time of flight spectrometer is used to record electron spectra generated by photoionization of Ne atoms (35), while for transient absorption studies, spectra of the transmitted through the cell attosecond pulse are recorded by a high-resolution XUV spectrometer installed downstream the gas cell.

3. Modeling the absorption of XUV pulses in Kr^+ in the presence of a strong NIR-field.

Femtosecond transient absorption dynamics, probed by a weak probe pulse in the presence of a pump pulse which affects the polarization response of the absorbing medium, have been at the center of various studies (38,51).

To explore these effects in the XUV, we model Kr^+ ions as a simplified three-level system depicted in Fig. S5. The first two states, hereafter referred to as $|1\rangle$ and $|2\rangle$, represent the ground $4p_{3/2}^{-1}$ and the excited $3d_{5/2}^{-1}$ states of the ion, respectively, i.e. the states associated with the $4p_{3/2}^{-1} \rightarrow 3d_{5/2}^{-1}$ transition.

To introduce the polarizability of state $|1\rangle$ of the Kr^+ ion, a third state $|3\rangle$ is included in the present considerations. The energy spacing between the states $|1\rangle$ and $|3\rangle$ is set to 13.5 eV and the corresponding transition matrix element to $\mu = 1.87 \cdot 10^{-29}$ C·m. Both values are calculated via the COWAN atomic structure code (52) and they describe the coupling between the $4p_{3/2}^{-1}$ and the $4s_{1/2}^{-1}$ ($4s4p^6$ electron configuration). The unperturbed transition energy $\hbar\omega_{12}$ equals 79.95 eV, i.e. that of the $4p_{3/2}^{-1} \rightarrow 3d_{5/2}^{-1}$ absorption resonance.

E_L, E_{XUV}, ω_L and ω_{XUV} denote the electric fields and the central frequencies of the light transient and that of the attosecond XUV pulse, respectively, while τ stands for their relative delay. The decay rate of state $|2\rangle$ is assumed to be $\Gamma_A \approx 1/7.5 \text{ fs}^{-1}$, which corresponds to an Auger decay time of the 3d hole of 7.5 fs (53). Strong-field ionization (SFI) in the Bloch model is introduced via an electric field dependent feeding rate $\Gamma_{SFI}(t)$ of the ground state, which is indicated schematically in Fig. S5. The ionization rate has been calculated from a fit of static field extracted values (54).

In all simulations, the field of the transient is the one evaluated by the streaking measurements (see Fig. 3B of the main publication) with the peak intensity adjusted to $\sim 4.8 \cdot 10^{14} \text{ W/cm}^2$. Similarly, the duration of the XUV pulse is set to 200 as and is spectrally centered at 80 eV.

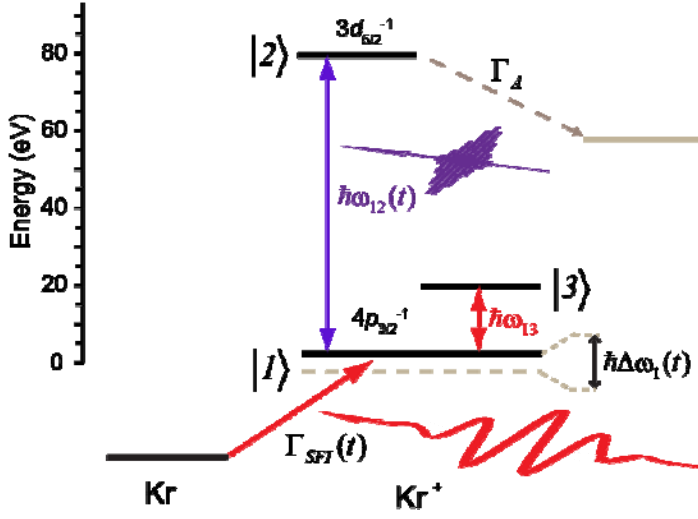


Fig. S5

Schematic diagram of the three-level system for modeling resonant XUV absorption of Kr^+ .

Due to the presence of the additional state $|3\rangle$, the ground state $|1\rangle$ is more susceptible to the light transient, which translates into a significant periodic variation of its energy (ac Stark effect), thereby rendering the probed transition frequency ω_2 time dependent:

$$\omega_{12}(t) = \omega_2 - \Delta\omega_1(t), \text{ where } \Delta\omega_1(t) = \sqrt{(\omega_{13} - \omega_L)^2 + 4\Omega_{13,L}(t)^2} + (\omega_L - \omega_{13}) \text{ and}$$

$$\Omega_{13,L}(t) = \frac{\mu_{13}E_L(t)}{\hbar} \text{ denotes the instantaneous Rabi frequency between the states } |1\rangle \text{ and } |3\rangle.$$

To calculate the absorption cross-section $\sigma(\omega, \tau)$ of the $|1\rangle \rightarrow |2\rangle$ transition, we numerically integrate the von Neumann equation:

$$i\hbar \frac{d\rho}{dt} = [H_0, \rho] - [\mu \cdot E_{IR}(t), \rho] - [\mu \cdot E_{XUV}(t - \tau), \rho] + i\hbar \left. \frac{d\rho}{dt} \right|_{SFI} + i\hbar \left. \frac{d\rho}{dt} \right|_{Relax}$$

with the unperturbed Hamiltonian H_0 , the dipole operator μ in the dipole approximation and the density matrix ρ :

$$H_0 = \hbar \begin{pmatrix} \omega_{13} & 0 & 0 \\ 0 & \omega_{12} & 0 \\ 0 & 0 & 0 \end{pmatrix}; \quad \mu = \begin{pmatrix} 0 & 0 & \mu_{31} \\ 0 & 0 & \mu_{21} \\ \mu_{13} & \mu_{12} & 0 \end{pmatrix}; \quad \rho = \begin{pmatrix} \rho_{33} & \rho_{32} & \rho_{31} \\ \rho_{23} & \rho_{22} & \rho_{21} \\ \rho_{13} & \rho_{12} & \rho_{11} \end{pmatrix}.$$

The term $\left. \frac{d\rho}{dt} \right|_{SFI}$ phenomenologically describes the population rate of the ionic ground state $|1\rangle$ via strong-field ionization of the neutral atom. The decay rate Γ_A of the excited state as well as the spontaneous emission from level $|3\rangle$ —which is assumed to be

infinitely long compared to characteristic scales of this experiment—is considered in the term $\left. \frac{d\rho}{dt} \right|_{\text{Relax}}$.

The radiating dipole is obtained through the equation of motion of the matrix elements as:

$$d(t, \tau) = \text{Tr}(\mu\rho(t)) = 2 \text{Re}(\mu_{12}\rho_{12}(t, \tau) + \mu_{13}\rho_{13}(t, \tau)) .$$

$$\text{Hence, the absorption cross-section can be written as } \sigma(\omega, \tau) = \frac{\omega}{c\epsilon_0} \text{Im} \left[\frac{d(\omega, \tau)}{E_{\text{XUV}}(\omega)} \right].$$

Results 1: Distortion of the resonant XUV absorption line

Using our model, we explore the effects of spectral distortion of the $4p_{3/2}^{-1} \rightarrow 3d_{5/2}^{-1}$ absorption resonance due to the pump-induced perturbations to the generated ions by our light field transients.

Fig. S6 shows simulated transient dynamics encoded in the spectra corresponding to the $4p_{3/2}^{-1} \rightarrow 3d_{5/2}^{-1}$ transition for delays chosen to match those as in Fig. 3Di)-iii) of the main text.

The calculated absorption cross-sections are convolved with a Gaussian function (~ 300 meV FWHM) to account for the finite spectrometer resolution. The good reproduction of essential features, i.e. the negative absorbance at lower energies as well as positive absorbance at higher energies with respect to the main resonance, and the dynamic evolution of the absorption line as a function of the delay, validate the approach of modeling krypton ions with a simplified three-level system and confirm that the Stark effect is the key phenomenon behind the observed time-dependent spectral features.

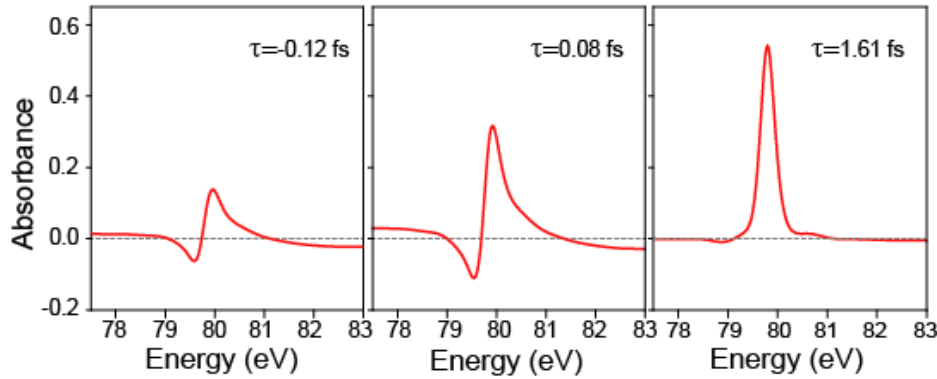


Fig. S6

Simulated absorbance spectra for the $4p_{3/2}^{-1} \rightarrow 3d_{5/2}^{-1}$ transition at three different delay instances, showing a good agreement with the corresponding experimental observation presented in Figs. 3D i)-iii). The finite spectrometer resolution is taken into account.

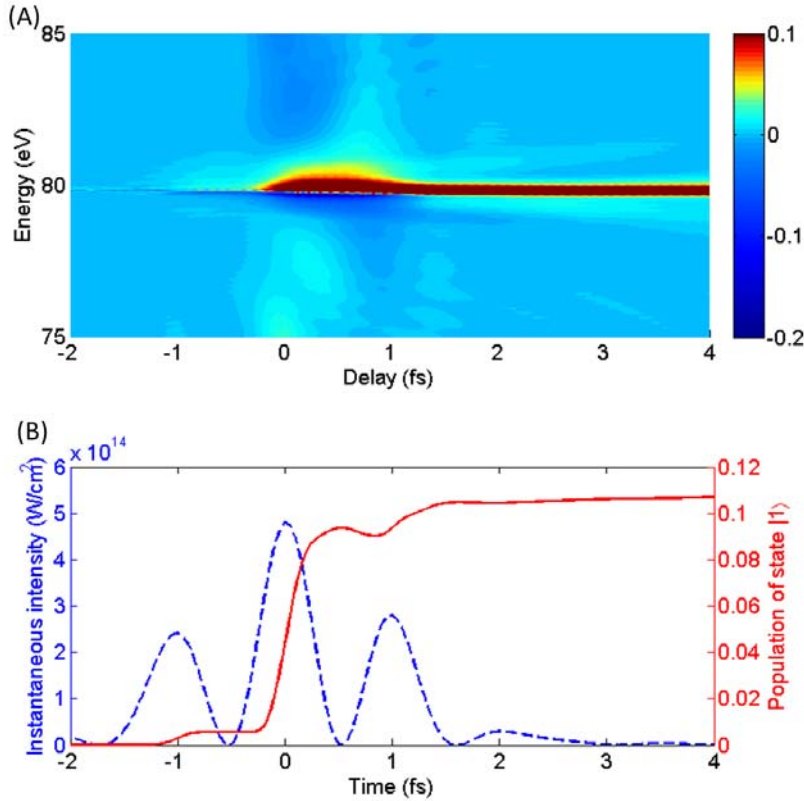


Fig. S7

Simulated transient absorbance spectra for an electric field dependent ionization rate $\Gamma_{SFI}(t)$ (A) and the underlying time dependent population of the ground state $|1\rangle$ (solid line) as well as the instantaneous intensity (dashed line) of the NIR laser pulse (B).

The false-color plot of Fig. S7A shows the calculated absorbance as a function of the pump-probe delay, while panel B depicts how the NIR field populates state $|1\rangle$ as a function of the delay, including the instantaneous intensity of the light transient.

In order to study how the lifetime of state $|2\rangle$ influences the distortion of the absorption in the presence of the NIR light field transient, the three-level system has been solved numerically for several lifetimes τ_A . Fig. S8 displays a series of absorbance spectrograms as a function of the pump-probe delay for a constant population $\left(\frac{d\rho}{dt}\Big|_{SFI} = 0\right)$,

where the lifetime τ_A was varied from 0.1 fs (panel A) to $\tau_{3d} = 7.5$ fs (panel E), the latter being the theoretical Auger lifetime of the $\text{Kr}^+ 3d^{-1}$ states (panel E).

For lifetimes significantly shorter than the half-period of the strong field, the emitting dipole undergoes (from (A) to (C)) a linear phase shift which is manifested by the characteristic modulation of its central energy at the double frequency of the pump field and corresponds to the (ac) Stark shift of state $|1\rangle$.

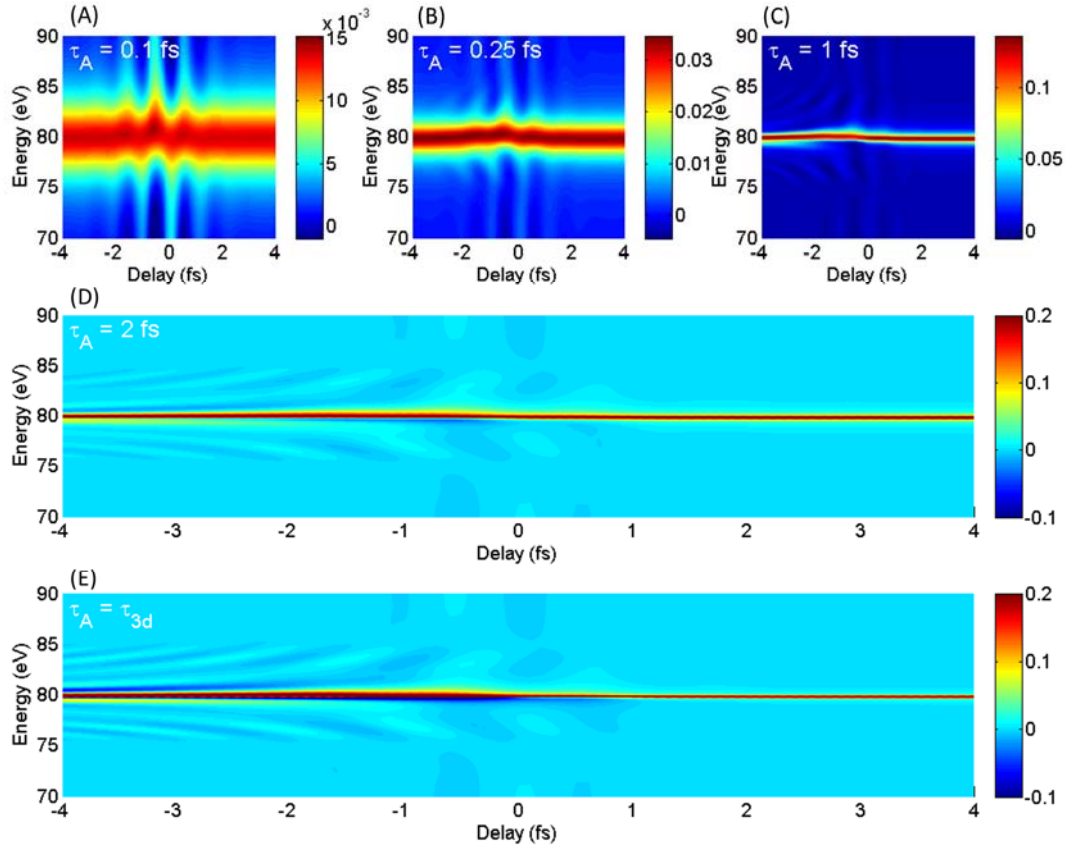


Fig. S8

The absorbance related to the $|1\rangle \rightarrow |2\rangle$ transition of Kr^+ ions computed as a function of the pump-probe delay for various settings of the lifetime τ_A of the excited state, as indicated in the upper left corner of each panel (assuming a static population). Graph (E) displays the simulated result for a lifetime equal to the $3d^{-1}$ hole decay time of Kr^+ .

For significantly longer lifetimes ((D) and (E)), the phase introduced to the emitting dipole encompasses the action of several field cycles and results in a line distortion rather than a pure shift of its central energy. Due to the steep leading edge of the XUV polarization—induced by our attosecond pulse—some signatures of the instantaneous Stark effect are expected to survive despite the effects introduced by the integration over the few fs long lifetime. This is demonstrated in Fig. S9, where the central energy of the resonance in the data shown in Fig. S8E has been evaluated by fitting a Lorentzian profile.

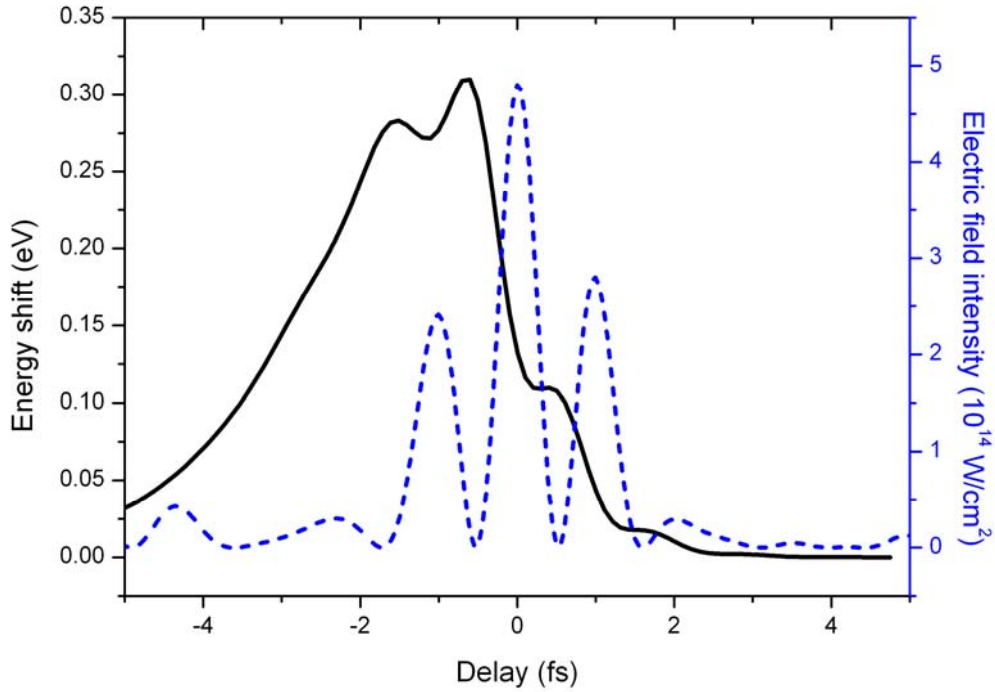


Fig. S9

Energy shift of the transition energy $\hbar\omega_{2}$ of the simulated absorption spectrogram as displayed in Fig. S8E (solid line) being analyzed by evaluating the central displacement of a fitted Lorentzian lineshape as a function of the delay τ . The blue dashed line shows the instantaneous intensity of the pump field.

Results 2: Strong-field ionization dynamics in the presence of pump polarization

Next, within our model, we attempt to accurately retrieve the population dynamics of the generated ions from an absorption spectrogram sampled under the conditions of our experiments.

Fig. S10 compares the ground state population of state $|1\rangle$, $\rho_{11}(t)$ (red curve), with that obtained by analyzing the simulated absorption spectra using the procedure described in section S4 of the SOM, which tracks the peak of the absorption line. The blue and green curves represent the retrieved populations based on our simulations with a 50 as and a 200 as XUV pulse, respectively. Note that the populations shown in Fig. S9 are based on an adiabatic tunnel-ionization model and therefore do not display the oscillatory behavior known from nonadiabatic calculations. The small “dip” in $\rho_{11}(t)$ at $t=0.8$ fs is due to the coupling between states $|1\rangle$ and $|3\rangle$. For the shorter XUV pulse (blue line), the ground-state population, estimated by tracking the peak of the absorption line, is significantly closer to $\rho_{11}(t)$. Since our experimental XUV probe pulse duration amounts to ~ 200 as, the present approach suggests that the technique of tracking the peak of the absorption

offers a possibility to recover the underlying population dynamics with an accuracy better than 10 %.

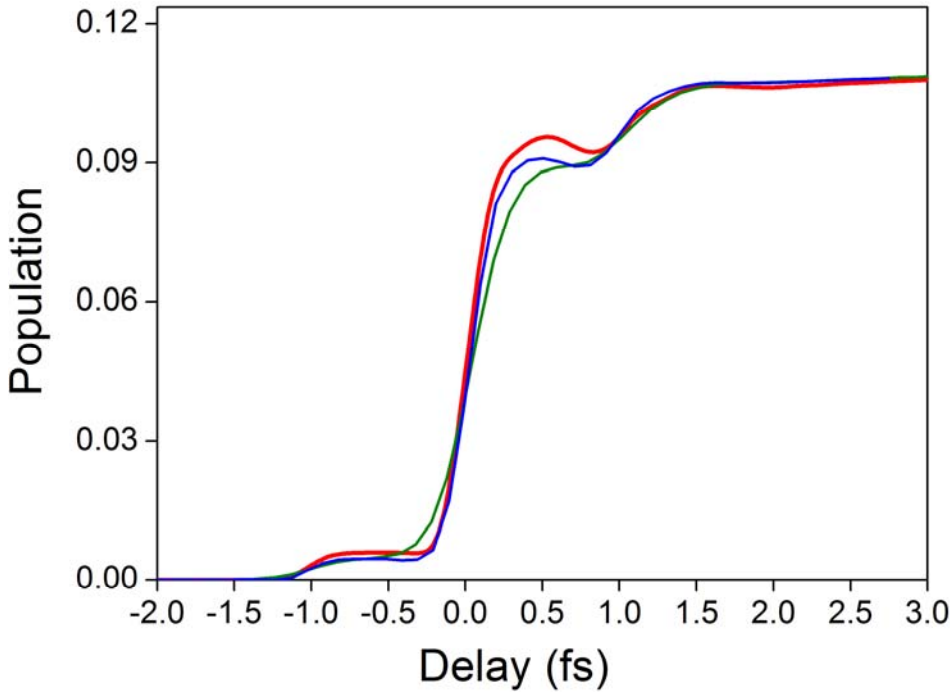


Fig. S10

Ground state population $\rho_{11}(t)$ derived by our model (red) and populations reconstructed by tracking the peak of the absorption line fitted with a Lorentzian profile. Blue (green) curve displays the retrieved population dynamics for an XUV probe pulse duration of 50 as (200 as).

4. Reconstruction of electron motion and determination of fractional ionization

Preparation of data prior to fitting

The absorbance spectrogram shown in Fig. 5A (in the main publication) was obtained by averaging over 12 consecutive scans, all taken under the same experimental conditions. All XUV spectra of the combined spectrogram were normalized in the spectral range from 83.0 - 86.7 eV (i.e. the high energy side next to the Kr^+ absorption lines) to reduce noise originating from flux variations of the XUV probe pulse. For calculating the absorbance $A(\omega, \tau)$, the mean spectral density in the time interval prior to ionization (-20.25 to -6.25 fs) has been used as a reference spectrum.

Fitting procedure

To reconstruct the Kr^+ quantum state distribution, the coherence of the spin-orbit wavepacket motion as well as the quantum phase, a fit of the experimental data shown in Fig. 5A is performed using the model equation

$$A(\omega, \tau) = -\ln \left[\exp[-n_0 \sigma(\omega, \tau)L] * G(\omega) \right] + A_0 \quad (\text{S1})$$

applied to the spectrogram. Here, $\sigma(\omega, \tau)$ is an analytical description of the cross-section of the three absorption lines of Kr^+ based on eq. (35) in (55) where the reported reduced transition matrix elements are employed. Furthermore, τ indicates the time of probing, $n_0 = 5.75 \cdot 10^{18} \text{ cm}^{-3}$ the initial number density of neutral atoms, $L = 0.74 \text{ mm}$ the length of the target cell and $G(\omega)$ an area-normalized Gaussian convolution function with Δ being the FWHM value characterizing the finite spectrometer resolution and A_0 a constant offset. The coherence term in $\sigma(\omega, \tau)$ is described by

$\rho_{3/2,1/2}^{(1/2)}(\tau) = \left| \rho_{3/2,1/2}^{(1/2)} \right| \exp(i\phi(\tau)) = \left| \rho_{3/2,1/2}^{(1/2)} \right| \exp(i\Delta E_{SO}\tau + i\delta)$, where ΔE_{SO} is the spin-orbit wavepacket splitting and δ is a phase offset which depends on the choice of the time origin $\tau = 0$ (atomic units $\hbar = e = m_e = a_0 = 1$ are used throughout this section). We chose $\tau = 0$ such that it coincides with the maximum of the instantaneous intensity of the synthesized light field transient. Hence, for a sufficiently short pump pulse, the quantity δ equals the initial quantum phase.

We fit the data set by employing the Levenberg-Marquardt optimization algorithm in the range 78.5 – 82 eV and for the delays 2.75 to 29.75 fs, avoiding the fit in the presence of the strong single-cycle initiation pulse since the model function (eq. (S1)) is not valid for describing XUV absorption under strong field influence. The fit parameters were the

populations ($\rho_{1/2,1/2}^{(1/2)}$, $\rho_{3/2,3/2}^{(1/2)}$, $\rho_{3/2,3/2}^{(3/2)}$), the terms describing the coherence

($\left| \rho_{3/2,1/2}^{(1/2)} \right|$, ΔE_{SO} , δ), the three central energies of the XUV transitions ($E_{3d_{5/2}} - E_{4p_{3/2}}$, $E_{3d_{3/2}} - E_{4p_{3/2}}$, $E_{3d_{3/2}} - E_{4p_{1/2}}$), as well as the spectrometer resolution Δ and the constant offset A_0 .

The sum of populations permits evaluation of the fractional ionization. The populations provided in the main publication are scaled to 100% fractional ionization.

Error analysis

Error bars of the fit quantities, reported in the main document, represent the standard error of fit results obtained by applying the described fitting approach to six consecutive pairs of the 12 delay scans. Besides the standard error, we have also calculated the standard deviations of the distributions, which on average yield values ~ 1.9 times larger than the standard error.

5. Retrieval of population during strong-field perturbation

Similar to the approach of fitting the absorption spectrogram after the NIR pump pulse, the formation of the population in the presence of the pump pulse has been addressed by fitting the transient absorption spectrogram using the model

$$A_p(\omega, \tau) = -\ln[\exp[-c(\omega, \tau)] * G(\omega)] + A_0(\tau),$$

where $G(\omega)$ and $A_0(\tau)$ are introduced above, and $c(\omega, \tau)$ describes the absorption lines by three Lorentzian lineshape functions:

$$c(\omega, \tau) \propto \frac{1}{2\pi} \sum_{i=1}^3 n_i(\tau) \frac{\Gamma}{(\omega - \omega_i(\tau))^2 + (\Gamma/2)^2}.$$

Here, the $n_i(\tau)$ denote the effective population and $\omega_i(\tau)$ represents the central frequency of the i^{th} absorption line.

For the experimental parameters, this approach has been proven to allow the retrieval of the population to within an accuracy of $\sim 10\%$ (see section S3).

The fit was carried out for the delay range of -20.25 to 29.75 fs and within the spectral window extending from 77.9 to 83 eV, where the results obtained in the range 2.75 to 29.75 fs served to scale the effective populations according to the determined population by utilizing eq. (S1).

All error bars in the main document depict standard errors (see section S3, *Error analysis*).

6. Numerical 3D-TDSE propagation

Theoretical modeling of strong-field ionization of the $4p$ sub-shell was done by numerically propagating the three-dimensional time-dependent Schrödinger equation (3D-TDSE) for a single active electron in the length gauge on a grid, using a standard technique (56). Assuming a spherically symmetric potential $V(r)$, and the experimental laser field $F(t)$ as shown in Fig. 3B polarized along the z -axis, the 3D-TDSE reads (in atomic units (a.u.): $\hbar = e = m_e = a_0 = 1$),

$$-\frac{1}{2}\Delta\psi(\vec{r}, t) + (V(|\vec{r}|) + F(t)z)\psi(\vec{r}, t) = i\frac{\partial}{\partial t}\psi(\vec{r}, t) \quad (\text{S2})$$

where Δ is the Laplace operator, and $\psi(\vec{r}, t)$ is the electron's wave function in coordinate space. Expanding the wave function in partial waves*,

$$\psi(\vec{r}, t) = \sum_{l=0}^L \frac{w_l(r, t)}{r} \sum_{m=-1}^1 Y_l^m(\theta, \varphi), \quad (\text{S3})$$

* The azimuthal quantum number m assumes only three values since the initial state is an orbital of the $4p$ sub-shell and the laser field preserves m due to the dipole selection rules, as evidenced by eq. (S6) and (S7).

allows us to write eq. (S2) as a set of coupled 1D radial Schrödinger equations with respect to the reduced radial wave functions $w_l(r, t)$:

$$\left(-\frac{1}{2} \frac{\partial^2}{\partial r^2} + B(r)\right) \bar{w}(r, t) + A(r, t) \bar{w}(r, t) = i \frac{\partial}{\partial t} \bar{w}(r, t), \quad (\text{S4})$$

$$\bar{w}(r, t) = \begin{bmatrix} w_1(r, t) \\ w_2(r, t) \\ \vdots \\ w_L(r, t) \end{bmatrix}, \quad (\text{S5})$$

$$B_{l,l'}(r) = \delta_{l,l'} \left(\frac{l(l+1)}{2r^2} + (2l+1) \begin{pmatrix} l & 0 & l \\ 0 & 0 & 0 \end{pmatrix} \begin{pmatrix} l & 0 & l \\ m & 0 & -m \end{pmatrix} V(r) \right), \quad (\text{S6})$$

$$A_{l,l'}(r, t) = \delta_{l\pm 1, l'} \sqrt{(2l+1)(2l'+1)} \begin{pmatrix} l' & 0 & l \\ 0 & 0 & 0 \end{pmatrix} \begin{pmatrix} l' & 0 & l \\ m & 0 & -m \end{pmatrix} rF(t), \quad (\text{S7})$$

where the tabulated quantities in eq. (S6) and (S7) are Wigner-3j symbols—they arise naturally here by angularly integrating products of three spherical harmonics—and $\delta_{l,l'}$ is the Kronecker symbol; $V(r)$ is a pseudopotential that reproduces the ionization energy of neutral Kr. Time-propagation of eq. (S4) was achieved using the following symmetric splitting scheme:

$$\bar{w}(r, t + \delta t) = U(t, t + \delta t) \bar{w}(r, t); \quad (\text{S8})$$

$$U(t, t + \delta t) = \left[1 + i \frac{\delta t}{2} \left(-\frac{1}{2} \frac{\partial^2}{\partial r^2} + B(r) \right) \right]^{-1} \left[1 + i \frac{\delta t}{2} A(r, t + \delta t / 2) \right]^{-1} \times \left[1 - i \frac{\delta t}{2} A(r, t + \delta t / 2) \right] \left[1 - i \frac{\delta t}{2} \left(-\frac{1}{2} \frac{\partial^2}{\partial r^2} + B(r) \right) \right]. \quad (\text{S9})$$

Numerical convergence is more difficult to achieve in the length gauge than in the velocity gauge due to (i) a larger number of partial waves components required to represent the wave function in the laser field and (ii) because the phases of the wave function's components at large radial distances change rapidly, requiring a finer time step to accurately propagate these. Nevertheless, we achieved numerical convergence using an angular momentum grid up to $L=100$, and time and radial grid steps of 0.007 a.u. and 0.03 a.u., respectively, with a radial grid extending to 1000 a.u.. We also included a radial absorbing potential starting at $r=750$ a.u. to delete any unphysical reflections from the wave functions at confines of the finite simulation box.

The amount of ionization at some time t due to the strong infrared field can be defined as (57)

$$P(t) = 1 - \sum_n \left| \langle \phi_n | \psi(t) \rangle \right|^2, \quad (\text{S10})$$

where the sum ranges over all bound states $\langle \phi_n |$ of the atom. However, calculations based on the atomic structure code (COWAN) (52) suggest that, excited neutrals would absorb XUV photons at approximately the same energy as Kr^+ ions. To account for this fact, we

limit the range of the summation in eq. (S10) to a sufficient number of bound states to ensure numerical convergence. In this way, Kr atoms excited to their Rydberg electronic states are considered as ions.

Now, since the numerical propagation of the 3D-TDSE was performed in the decoupled spin-orbit basis $|(ls)m_l m_s\rangle = |(1/2)m_l m_s\rangle := |m_l m_s\rangle$, while the measured absorption lines resolve populations in the coupled spin-orbit basis

$|(ls)JM\rangle = |(1/2)JM\rangle := |JM\rangle$ — $J(J+1)$ being the eigenvalue of $J^2 = (\vec{L} + \vec{S})^2$ — we evaluate $P(t)$ as

$$P(t) = 1 - \sum_{n,l,m_l,m_s} \left| \langle m_l m_s | JM \rangle \int_0^\infty dr \phi_{nl}(r) w_l(r,t) \right|^2,$$

where $\langle m_l m_s | JM \rangle$ is a Clebsch-Gordan coefficient and $\phi_{nl}(r)$ is the reduced radial wave function of a bound state with principal quantum number n and orbital quantum number l , obtained by solving the time-independent radial Schrödinger equation

$$-\frac{1}{2} \frac{\partial^2}{\partial r^2} \phi_{nl}(r) + \left(\frac{l(l+1)}{2r^2} + V(r) \right) \phi_{nl}(r) = \varepsilon_n \phi_{nl}(r).$$

7. TDCIS simulations and predictions for the valence electron dynamics of Kr^+

We model the strong-field ionized ensemble of krypton ions by utilizing our pioneering 3D time-dependent configuration-interaction singles (TDCIS) approach (43), which systematically captures correlations in photoionization processes.

Within the TDCIS approach, the Coulomb interaction between the NIR-generated hole state and the NIR-generated photoelectron is treated exactly. This interaction leads subsequently to correlation and to an entangled state between the parent ion and the photoelectron (58).

In this work, we extended our TDCIS approach (43) to account for spin-orbit interaction and spin-orbit driven valence electron wavepacket motion (44). To be able to simulate the strong-field ionization processes, a large range of the continuum spectrum must be covered with the need to cover angular momentum states up to $L=60$. To account for the multi-electron dynamics that can originate from several orbitals, we consider 18 spin orbitals ranging from $3d_{3/2}$ to $4p_{3/2}$. The total number of electronic configurations lies above 250 000, which is computationally a very challenging task.

The results of our simulations for the condition of the experiment yield the populations: $\rho_{3/2,3/2}^{(3/2)} + \rho_{3/2,3/2}^{(-3/2)} = 0.06$, $\rho_{3/2,3/2}^{(1/2)} + \rho_{3/2,3/2}^{(-1/2)} = 0.74$, $\rho_{1/2,1/2}^{(1/2)} + \rho_{1/2,1/2}^{(-1/2)} = 0.20$ (scaled to 100% fractional ionization) and a degree of coherence of $g = 0.72$, which are in good agreement with the experimental observations. Propagation effects of the EUV pulse in the medium can lead to modifications in the observed spectrum resulting in an apparent

ion density matrix that differs from the actual ion density matrix. In particular, the off-diagonal elements and, hence, the apparent hole coherence are affected by propagation effects. Based on previous theoretical work (54), we find that the apparent degree of coherence can be overestimated by up to 14 %. Applying this result to our theoretical prediction, we would expect an apparent degree of coherence of 0.82, which is in remarkable agreement with $g = 0.85 \pm 0.06$ retrieved from the experiment. The only open question that remains, is the discrepancy between the relative populations of the $m_j = \pm 3/2$ and $m_j = \pm 1/2$ states in the $j = 3/2$ manifold. This might indicate the need to include correlation effects that cannot be described by the TDCIS approach.

8. Delay correction between streaking and transient absorption spectrograms

Strong-field ionization, as studied in our attosecond transient absorption experiments, requires field intensities on the order of 10^{14} W/cm² and beyond. In contrast, streaking measurements of the light waveforms require intensities on the order of 10^{12} W/cm². In our experiments, the intensity of the laser beam is varied by adjusting its size with an adjustable aperture placed before the focusing mirror. The >10-fold increase of the illuminated area of the mirror between a streaking and a transient absorption (TA) measurement can be responsible for spatiotemporal effects, particularly a delay between the weak (streaking) and the strong (TA) pulse, which must be corrected before comparing the streaking and transient absorption measurements with respect to one and the same delay axis.

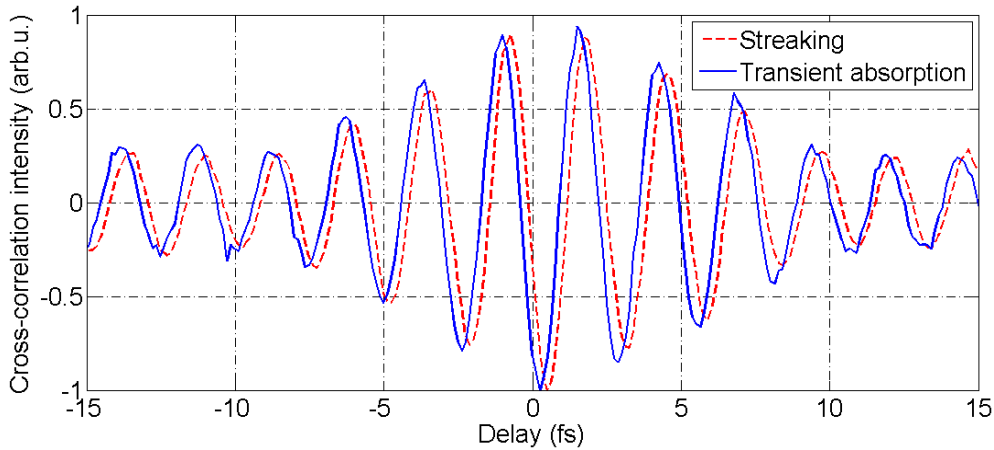


Fig. S11

Variation of the focal point intensity in a cross-correlation measurement obtained under streaking (red dashed curve) and transient absorption (blue solid line) intensity settings. An evaluation of the delay yields (280 ± 50) as.

This effect has been investigated by removing the metallic filter of the pellicle used in the experiments and recording the linear cross-correlation trace between the central part of the NIR beam, and the portion reflected off the outer mirror for two different radii of

illumination, corresponding to those of the streaking and TA measurements accordingly. Fig. S11 shows the variation of the intensity at the focal point of the beams imaged on a CCD camera (averaged over 5×5 pixels covering the central part of the beam) as a function of the delay between inner and outer mirror.

The delay between the two traces is evaluated by a linear fit of the spectral phases of both signals and amounts to (280 ± 50) as. This apparent delay, which is taken into account for the synchronous display of fields, can be attributed to simple geometrical effects introduced by spherical aberrations. The geometrical delay, evaluated at the focal plane, in the time of arrival between two pulses traveling along off-axis rays at a distance r from the mirror axis and on-axis pulses, for a spherical mirror of radius R (59), is given by

$$\Delta T(r) = \frac{3}{4} \frac{R}{c} \left(\frac{r}{R} \right)^4.$$

For a pulse reflected by an annular portion of a spherical mirror situated between radii r_1 and r_2 , the introduced delay (assuming a constant spatial intensity distribution) can be expressed as:

$$\begin{aligned} {}_{r_1}^{r_2} \Delta T &= \frac{\frac{3}{4} \frac{R}{c} \int_0^{2\pi} \int_{r_1}^{r_2} \left(\frac{r}{R} \right)^4 r \, dr \, d\theta}{\int_0^{2\pi} \int_{r_1}^{r_2} r \, dr \, d\theta} \\ \Rightarrow {}_{r_1}^{r_2} \Delta T &= \frac{1}{4} \frac{R}{c} \frac{1}{R^4} \frac{(r_2^6 - r_1^6)}{(r_2^2 - r_1^2)}. \end{aligned}$$

For a mirror with $R = 250$ mm, an inner mirror radius $r_1 \approx 1.5$ mm and a streaking (TA) beam radius of $r_2 \approx 2.5$ mm ($r_2 \approx 8.1$ mm), the latter expression yields an effective delay between the streaking and transient absorption spectrograms of 240 as, which is in excellent agreement with the delay evaluated from the data shown in Fig. S11.

References and Notes

1. J. F. Whitaker *et al.*, External electro-optic integrated circuit probing. *Microelectron. Eng.* **12**, 369 (1990). [doi:10.1016/0167-9317\(90\)90050-4](https://doi.org/10.1016/0167-9317(90)90050-4)
2. L. Xu *et al.*, Route to phase control of ultrashort light pulses. *Opt. Lett.* **21**, 2008 (1996). [doi:10.1364/OL.21.002008](https://doi.org/10.1364/OL.21.002008) [Medline](#)
3. T. Brabec, F. Krausz, Intense few-cycle laser fields: Frontiers of nonlinear optics. *Rev. Mod. Phys.* **72**, 545 (2000). [doi:10.1103/RevModPhys.72.545](https://doi.org/10.1103/RevModPhys.72.545)
4. J. Reichert *et al.*, Measuring the frequency of light with mode-locked lasers. *Opt. Commun.* **172**, 59 (1999). [doi:10.1016/S0030-4018\(99\)00491-5](https://doi.org/10.1016/S0030-4018(99)00491-5)
5. D. J. Jones *et al.*, Carrier-envelope phase control of femtosecond mode-locked lasers and direct optical frequency synthesis. *Science* **288**, 635 (2000). [doi:10.1126/science.288.5466.635](https://doi.org/10.1126/science.288.5466.635) [Medline](#)
6. S. A. Diddams *et al.*, Direct link between microwave and optical frequencies with a 300 THz femtosecond laser comb. *Phys. Rev. Lett.* **84**, 5102 (2000). [doi:10.1103/PhysRevLett.84.5102](https://doi.org/10.1103/PhysRevLett.84.5102) [Medline](#)
7. A. Apolonski *et al.*, Controlling the phase evolution of few-cycle light pulses. *Phys. Rev. Lett.* **85**, 740 (2000). [doi:10.1103/PhysRevLett.85.740](https://doi.org/10.1103/PhysRevLett.85.740) [Medline](#)
8. T. Udem, R. Holzwarth, T. W. Hänsch, Optical frequency metrology. *Nature* **416**, 233 (2002). [doi:10.1038/416233a](https://doi.org/10.1038/416233a) [Medline](#)
9. S. T. Cundiff, J. Ye, Colloquium: Femtosecond optical frequency combs. *Rev. Mod. Phys.* **75**, 325 (2003). [doi:10.1103/RevModPhys.75.325](https://doi.org/10.1103/RevModPhys.75.325)
10. A. Baltuška *et al.*, Attosecond control of electronic processes by intense light fields. *Nature* **421**, 611 (2003). [doi:10.1038/nature01414](https://doi.org/10.1038/nature01414) [Medline](#)
11. M. Hentschel *et al.*, Attosecond metrology. *Nature* **414**, 509 (2001). [doi:10.1038/35107000](https://doi.org/10.1038/35107000) [Medline](#)
12. R. Kienberger *et al.*, Atomic transient recorder. *Nature* **427**, 817 (2004). [doi:10.1038/nature02277](https://doi.org/10.1038/nature02277) [Medline](#)
13. G. Sansone *et al.*, Isolated single-cycle attosecond pulses. *Science* **314**, 443 (2006). [doi:10.1126/science.1132838](https://doi.org/10.1126/science.1132838) [Medline](#)
14. E. Goulielmakis *et al.*, Single-cycle nonlinear optics. *Science* **320**, 1614 (2008). [doi:10.1126/science.1157846](https://doi.org/10.1126/science.1157846) [Medline](#)
15. M. F. Kling *et al.*, Control of electron localization in molecular dissociation. *Science* **312**, 246 (2006). [doi:10.1126/science.1126259](https://doi.org/10.1126/science.1126259) [Medline](#)
16. G. Sansone *et al.*, Electron localization following attosecond molecular photoionization. *Nature* **465**, 763 (2010). [doi:10.1038/nature09084](https://doi.org/10.1038/nature09084) [Medline](#)
17. M. Schultze *et al.*, Delay in photoemission. *Science* **328**, 1658 (2010). [doi:10.1126/science.1189401](https://doi.org/10.1126/science.1189401) [Medline](#)

18. J. Mauritsson *et al.*, Attosecond electron spectroscopy using a novel interferometric pump-probe technique. *Phys. Rev. Lett.* **105**, 053001 (2010).
[doi:10.1103/PhysRevLett.105.053001](https://doi.org/10.1103/PhysRevLett.105.053001) [Medline](#)
19. E. Goulielmakis *et al.*, Real-time observation of valence electron motion. *Nature* **466**, 739 (2010). [doi:10.1038/nature09212](https://doi.org/10.1038/nature09212) [Medline](#)
20. S. Zherebtsov *et al.*, *Nat. Phys.* (2011). [10.1038/nphys1983](https://doi.org/10.1038/nphys1983)
21. P. Eckle *et al.*, Attosecond ionization and tunneling delay time measurements in helium. *Science* **322**, 1525 (2008). [doi:10.1126/science.1163439](https://doi.org/10.1126/science.1163439) [Medline](#)
22. S. E. Harris, A. V. Sokolov, Subfemtosecond Pulse Generation by Molecular Modulation. *Phys. Rev. Lett.* **81**, 2894 (1998). [doi:10.1103/PhysRevLett.81.2894](https://doi.org/10.1103/PhysRevLett.81.2894)
23. A. V. Sokolov, D. R. Walker, D. D. Yavuz, G. Y. Yin, S. E. Harris, Raman generation by phased and antiphased molecular states. *Phys. Rev. Lett.* **85**, 562 (2000).
[doi:10.1103/PhysRevLett.85.562](https://doi.org/10.1103/PhysRevLett.85.562) [Medline](#)
24. J. Q. Liang, M. Katsuragawa, F. L. Kien, K. Hakuta, Sideband generation using strongly driven raman coherence in solid hydrogen. *Phys. Rev. Lett.* **85**, 2474 (2000).
[doi:10.1103/PhysRevLett.85.2474](https://doi.org/10.1103/PhysRevLett.85.2474) [Medline](#)
25. A. V. Sokolov, D. R. Walker, D. D. Yavuz, G. Y. Yin, S. E. Harris, Femtosecond light source for phase-controlled multiphoton ionization. *Phys. Rev. Lett.* **87**, 033402 (2001).
[doi:10.1103/PhysRevLett.87.033402](https://doi.org/10.1103/PhysRevLett.87.033402) [Medline](#)
26. T. Suzuki, M. Hirai, M. Katsuragawa, Octave-spanning Raman comb with carrier envelope offset control. *Phys. Rev. Lett.* **101**, 243602 (2008).
[doi:10.1103/PhysRevLett.101.243602](https://doi.org/10.1103/PhysRevLett.101.243602) [Medline](#)
27. Z.-M. Hsieh *et al.*, Controlling the carrier-envelope phase of Raman-generated periodic waveforms. *Phys. Rev. Lett.* **102**, 213902 (2009). [doi:10.1103/PhysRevLett.102.213902](https://doi.org/10.1103/PhysRevLett.102.213902)
[Medline](#)
28. H.-S. Chan *et al.*, Synthesis and measurement of ultrafast waveforms from five discrete optical harmonics. *Science* **331**, 1165 (2011). [doi:10.1126/science.1198397](https://doi.org/10.1126/science.1198397) [Medline](#)
29. R. K. Shelton *et al.*, Phase-coherent optical pulse synthesis from separate femtosecond lasers. *Science* **293**, 1286 (2001). [doi:10.1126/science.1061754](https://doi.org/10.1126/science.1061754) [Medline](#)
30. M. Yamashita, K. Yamane, R. Morita, Quasi-automatic phase-control technique for chirp compensation of pulses with over-one-octave bandwidth-generation of few- to mono-cycle optical pulses. *IEEE J. Sel. Top. Quantum Electron.* **12**, 213 (2006).
[doi:10.1109/JSTQE.2006.871961](https://doi.org/10.1109/JSTQE.2006.871961)
31. S. Rausch, T. Binhammer, A. Harth, F. X. Kärtner, U. Morgner, Few-cycle femtosecond field synthesizer. *Opt. Express* **16**, 17410 (2008). [doi:10.1364/OE.16.017410](https://doi.org/10.1364/OE.16.017410) [Medline](#)
32. G. Krauss *et al.*, Synthesis of a single cycle of light with compact erbium-doped fibre technology. *Nat. Photonics* **4**, 33 (2010). [doi:10.1038/nphoton.2009.258](https://doi.org/10.1038/nphoton.2009.258)
33. K. Okamura, T. Kobayashi, Octave-spanning carrier-envelope phase stabilized visible pulse with sub-3-fs pulse duration. *Opt. Lett.* **36**, 226 (2011). [doi:10.1364/OL.36.000226](https://doi.org/10.1364/OL.36.000226)
[Medline](#)

34. E. Goulielmakis *et al.*, Attosecond control and measurement: lightwave electronics. *Science* **317**, 769 (2007). [doi:10.1126/science.1142855](https://doi.org/10.1126/science.1142855) [Medline](#)
35. E. Goulielmakis *et al.*, Direct measurement of light waves. *Science* **305**, 1267 (2004). [doi:10.1126/science.1100866](https://doi.org/10.1126/science.1100866) [Medline](#)
36. indicates that relative to the ground state configuration a hole (or electron vacancy) is created in the $nl_j^{-1} nl$ sub-shell, where j denotes the total angular momentum and m_j its projection on the z axis, the latter being aligned with the laser polarization.
37. B. R. Mollow, Absorption and Emission Line-Shape Functions for Driven Atoms. *Phys. Rev. A* **5**, 1522 (1972). [doi:10.1103/PhysRevA.5.1522](https://doi.org/10.1103/PhysRevA.5.1522)
38. T. Unold, K. Mueller, C. Lienau, T. Elsaesser, A. D. Wieck, Optical Stark effect in a quantum dot: ultrafast control of single exciton polarizations. *Phys. Rev. Lett.* **92**, 157401 (2004). [doi:10.1103/PhysRevLett.92.157401](https://doi.org/10.1103/PhysRevLett.92.157401) [Medline](#)
39. C. H. B. Cruz, J. P. Gordon, P. C. Becker, R. L. Fork, C. V. Shank, *Int. J. Quant. Elec.* **24**, 261 (1988). [doi:10.1109/3.122](https://doi.org/10.1109/3.122)
40. S. H. Autler, C. H. Townes, Stark Effect in Rapidly Varying Fields. *Phys. Rev.* **100**, 703 (1955). [doi:10.1103/PhysRev.100.703](https://doi.org/10.1103/PhysRev.100.703)
41. B. J. Sussman, Five ways to the nonresonant dynamic Stark effect. *Am. J. Phys.* **79**, 477 (2011). [doi:10.1119/1.3553018](https://doi.org/10.1119/1.3553018)
42. N. B. Delone, V. P. Krainov, AC Stark shift of atomic energy levels. *Phys. Uspekhi* **169**, 753 (1999). [doi:10.3367/UFNr.0169.199907c.0753](https://doi.org/10.3367/UFNr.0169.199907c.0753)
43. L. Greenman *et al.*, Implementation of the time-dependent configuration-interaction singles method for atomic strong-field processes. *Phys. Rev. A* **82**, 023406 (2010). [doi:10.1103/PhysRevA.82.023406](https://doi.org/10.1103/PhysRevA.82.023406)
44. S. Pabst, L. Greenman, P. J. Ho, D. A. Mazziotti, R. Santra, Decoherence in attosecond photoionization. *Phys. Rev. Lett.* **106**, 053003 (2011). [doi:10.1103/PhysRevLett.106.053003](https://doi.org/10.1103/PhysRevLett.106.053003) [Medline](#)
45. F. Remacle, M. Nest, R. D. Levine, Laser steered ultrafast quantum dynamics of electrons in LiH. *Phys. Rev. Lett.* **99**, 183902 (2007). [doi:10.1103/PhysRevLett.99.183902](https://doi.org/10.1103/PhysRevLett.99.183902) [Medline](#)
46. M. Meckel *et al.*, Laser-induced electron tunneling and diffraction. *Science* **320**, 1478 (2008). [doi:10.1126/science.1157980](https://doi.org/10.1126/science.1157980) [Medline](#)
47. O. Smirnova *et al.*, High harmonic interferometry of multi-electron dynamics in molecules. *Nature* **460**, 972 (2009). [doi:10.1038/nature08253](https://doi.org/10.1038/nature08253) [Medline](#)
48. M. Gertsvolf, M. Spanner, D. M. Rayner, P. B. Corkum, Demonstration of attosecond ionization dynamics inside transparent solids. *J. Phys. B* **43**, 131002 (2010). [doi:10.1088/0953-4075/43/13/131002](https://doi.org/10.1088/0953-4075/43/13/131002)
49. M. Durach, A. Rusina, M. F. Kling, M. I. Stockman, Metallization of nanofilms in strong adiabatic electric fields. *Phys. Rev. Lett.* **105**, 086803 (2010). [doi:10.1103/PhysRevLett.105.086803](https://doi.org/10.1103/PhysRevLett.105.086803) [Medline](#)

50. V. Pervak, Recent development and new ideas in the field of dispersive multilayer optics. *Appl. Opt.* **50**, (Issue 9), C55 (2011). [doi:10.1364/AO.50.000C55](https://doi.org/10.1364/AO.50.000C55) [Medline](#)
51. K. Misawa, K. Minoshima, T. Kobayashi, Femtosecond inverse Raman spectrum of molecular J-aggregates. *J. Raman Spec.* **26**, 553 (1995). [doi:10.1002/jrs.1250260710](https://doi.org/10.1002/jrs.1250260710)
52. R. D. Cowan, The theory of atomic structure and spectra, University of California Press, Ltd. (1981).
53. M. Jurvansuu, A. Kivimäki, S. Aksela, Inherent lifetime widths of Ar $2p^{-1}$, Kr $3d^{-1}$, Xe $3d^{-1}$, and Xe $4d^{-1}$ states. *Phys. Rev. A* **64**, 012502 (2001). [doi:10.1103/PhysRevA.64.012502](https://doi.org/10.1103/PhysRevA.64.012502)
54. R. Santra, R. Dunford, L. Young, Spin-orbit effect on strong-field ionization of krypton. *Phys. Rev. A* **74**, 043403 (2006). [doi:10.1103/PhysRevA.74.043403](https://doi.org/10.1103/PhysRevA.74.043403)
55. R. Santra, V. Yakovlev, T. Pfeifer, Z.-H. Loh, Theory of attosecond transient absorption spectroscopy of strong-field-generated ions. *Phys. Rev. A* **83**, 033405 (2011). [doi:10.1103/PhysRevA.83.033405](https://doi.org/10.1103/PhysRevA.83.033405)
56. H. G. Muller, *Laser Phys.* **9**, 138 (1999).
57. O. Smirnova, M. Spanner, M. Ivanov, Coulomb and polarization effects in sub-cycle dynamics of strong-field ionization. *J. Phys. At. Mol. Opt. Phys.* **39**, S307 (2006). [doi:10.1088/0953-4075/39/13/S05](https://doi.org/10.1088/0953-4075/39/13/S05)
58. N. Rohringer, R. Santra, Multichannel coherence in strong-field ionization. *Phys. Rev. A* **79**, 053402 (2009). [doi:10.1103/PhysRevA.79.053402](https://doi.org/10.1103/PhysRevA.79.053402)
59. J.-C. Diels, W. Rudolph, Ultrashort Laser Pulse Phenomenon: Fundamentals, techniques and applications on a femtosecond time scale, Academic Press, Boston, (1996).

Acknowledgments: We acknowledge the development of dedicated attosecond soft X-ray optics by Michael Hofstetter and Ulf Kleineberg (LMU, MPQ). Supported by the Max Planck Society, the ERC grant (Attoelectronics-258501), the DFG Cluster of Excellence: Munich Centre for Advanced Photonics (www.munich-photonics.de), the King Saud University–Max-Planck-Institut für Quantenoptik collaboration and the European Research Training Network ATTOFEL.